On the Characterization of Intermediate Scale Ionospheric Structure

Charles Rino[1] and Charles Carrano[1]

[1]Institute for Scientific Research, Boston College

Key Points:

- Least-squares and maximum likelihood irregularity parameter estimates generate correlated irregularity turbulent strength and spectral index parameter errors.
- Such correlations have been incorrectly interpreted as equatorial ionospheric structure characteristics.
- An improved maximum-likelihood estimation procedure is introduced that reduces the estimated parameter errors to negligible levels.

Corresponding author: Charles Rino, `crino@bc.edu`

Abstract

Stochastic ionospheric structure is characterized by three-dimensional spectral density functions (SDFs) constrained to reproduce the known structure correlation along magnetic field lines. In-situ diagnostics are formally one-dimensional scans of the structure. Thus, characterization of ionospheric structure starts with spectral analysis of one-dimensional time series. Theoretical models provide analytic relations between measured one-dimensional SDFs and the higher dimensional SDFs that characterize the structure. Unknown SDF parameters are estimated by model-fitting procedures, which will be referred to in this paper collectively as irregularity parameter estimation (IPE).

If the diagnostic SDF has the form $\Phi(q) = C_s q^{-\eta}$, where q is the spatial frequency, the logarithmic transformation $\log(\Phi(q)) = \log(C_s) - \eta \log(q)$ can be exploited to estimate $\log(C_s)$ and η. In this paper simulations are used to investigate LLE estimates of diagnostic single-component and two-component power-law SDFs. There is a known C_s bias and a more troublesome correlation between the $\log(C_s)$ and η estimates, which is exaggerated by unconstrained wavelet-based estimates. We found that this intrinsic property of LLE estimators completely explains a similar correlation long observed in both in-situ and radio propagation ionospheric diagnostic measurements.

More recent results have exploited the fact that the probability distribution function (PDF) of periodograms about the true mean is asymptotically χ_D. The conditional PDF is used to construct MLE estimates. The MLE estimates eliminate the bias, but the correlation persists. Recognizing that correlation between turbulent strength spectral index estimates is an intrinsic measurement property, error minimization is particularly important. A modified MLE procedure is presented that provides robust initiation and good error performance.

1 Introduction

The principal metric for characterizing ionospheric structure is the spectral density function (SDF), which is formally the expectation of the intensity of a spatial Fourier decomposition of the structure. Ionospheric structure is highly elongated along the direction of the earth's magnetic field, whereby stochastic variation is manifest only in planes that intercept field lines. Structure models project the two-dimensional structure onto measurable one-dimensional SDFs. Model development has been stimulated by recent physics-based high-resolution equatorial plasma bubble (EPS) simulations *Yokoyama* [2017] and by new propagation-theory results *Carrano and Rino* [2016]. The EPB simulations can be used to measure the intermediate scale structure directly. The propagation-theory results relate measured one-dimensional scintillation intensity SDFs to the path-integrated SDFs that generated the scintillation. In effect, the propagation diagnostics can be related directly to equivalent path-integrated structure models.

Model-data comparisons require conversions of measurement-specific time series to scan distance. Knowledge of the probe motion and structure drift is sufficient for in-situ diagnostics. Knowledge of the location and motion of a reference coordinate system are necessary for propagation diagnostics in addition to the structure drift. Either way, the scaling and geometric transformations can be absorbed in an effective velocity such that

$$y(t) = v_{eff}(t - t_0), \tag{1}$$

Consequently, only spectral analysis of spatially varying data segments need be considered.

Finally, by hypothesizing a parameterized analytic SDF form, the structure classification problem is reduced to estimating a small number of defining parameters. The two-component power-law model

$$\Phi(q) = C_s \begin{cases} q^{-\eta_1} & for \quad q \le q_0 \\ q_0^{\eta_2-\eta_1} q^{-\eta_2} & for \quad q > q_0 \end{cases}, \tag{2}$$

where q is the spatial wavenumber in radians per meter, is sufficient for characterizing intermediate-scale ionospheric structure. A two-component SDF functionally similar to (2) was introduced by *Carrano and Rino* [2016] to characterize the path-integrated phase SDF, which is not directly measurable. A compact theory was developed to predict the scintillation intensity SDF as a function of the path-integrated phase parameters. Here we consider direct estimation of power-law parameters. The notation C_s and η_n is used to distinguish the in-situ parameters from the propagation diagnostic parameters C_p and p_n.

If the theoretical SDF is a multi-component power-law, the simplest approach to power-law SDF parameter estimation exploits logarithmic transformation of the spectral estimates. The procedure was used to analyze in-situ data from the C/NOFS satellite *Rino et al.* [2016]. Wavelet-based estimators were used in part to identify homogeneous data segments, but also because wavelet estimators are well matched to power-law processes. The following correlation between the estimated η_1 and C_s and parameters was noted in the C/NOFS study:

$$\eta_1 = -0.02(C_s dB - C_0 dB). \tag{3}$$

The notation $C_s dB$ means $10\log_{10}(C_s)$. The $C_s dB - \eta_1$ correlation has also been observed in propagation diagnostics *Rino et al.* [1981], *Livingston et al.* [1981].

Recent studies of single-power-law LLE and MLE parameter estimation by *Vaughan* [2005], *Vaughan* [2010] and *Barret and Vaughan* [2011] show that the correlation represented by (3) is an intrinsic property of power-law parameter estimation. Moreover, although wavelet-based estimators are more accurate than periodogram estimators at higher frequencies, errors rapidly build up in the low-frequency range. The frequency dependence of the wavelet error distribution exaggerates the $C_s dB - \eta_1$ correlation. In light of these findings this paper reviews and extends power-law parameter estimation procedures.

2 Spectral Analysis Theory Summary

Estimating parameters that define the SDF of a power-law processes begins with an SDF estimate. Periodogram-based spectral estimation is well established for this purpose. The periodogram of the data sequence, $F_k = F(k\Delta y)$, for $k = 0, 1, \cdots, N-1$ is defined as

$$P_n = \frac{1}{N}\left|\widehat{F}_n\right|^2, \tag{4}$$

where

$$\widehat{F}_n = \sum_{k=0}^{N-1} F_k \exp\{-ink/N\} \tag{5}$$

is the discrete Fourier transform. From the relation

$$\frac{1}{N}\sum_{k=0}^{N-1} F_k^2 = \frac{1}{N}\sum_{n=0}^{N-1} P_n, \tag{6}$$

it follows that

$$\frac{1}{N}\sum_{k=0}^{N-1} \langle F_k^2 \rangle = \int \Phi(q)\frac{dq}{2\pi}, \tag{7}$$

where the angle brackets denote expectation, and $\Phi(q)$ is the SDF.

A standard procedure is used to generate realizations of F_k, namely

$$F_k = \sum_{n=0}^{N-1} \sqrt{\Phi(n\Delta q)\Delta q/\left(2\pi\right)}\zeta_n \exp\left\{ink/N\right\}, \tag{8}$$

where$\Delta q = 2\pi/(N\Delta y)$, and ζ_n is a zero mean Gaussian process with the white-noise property

$$\langle \zeta_n \zeta_n' \rangle = \begin{cases} 1 \text{ for } n = n \\ 0 \text{ for } n \neq n' \end{cases} \tag{9}$$

Substituting (8) into (5) it follows that

$$\left\langle |\widehat{F}_n|^2 \right\rangle = \Phi(n\Delta q)\Delta q/\left(2\pi\right), \tag{10}$$

and from (7)

$$\langle P_n \rangle N\Delta q/2\pi = \Phi(n\Delta q), \tag{11}$$

whereby a properly scaled periodogram is an unbiased estimate of the SDF.

Now consider the average

$$y = \frac{1}{M}\sum_{l=1}^{M} \widehat{\Phi}_n^{(l)}, \tag{12}$$

where $\widehat{\Phi}_n^{(l)}$ is a scaled periodogram estimate of a process with SDF Φ_n. By construction, F_k and $\widehat{F}_n$ are Gaussian random processes. For Gaussian random processes the summation of M intensity measurements has a known distribution:

$$P(y) = \frac{y^{M-1}\exp\left\{-y/\left(\Phi_n/M\right)\right\}}{\left(\Phi_n/M\right)^M \Gamma\left(M\right)}. \tag{13}$$

As described in *Appourchaux* [2003], the complex process that generates the realizations has 2 degrees of freedom per realization, which is accommodated in (13). From (13) the moments,$\langle I^m \rangle$, and the fractional moments, $F_m = \langle I^m \rangle / \langle I \rangle^m$, can be computed:

$$\langle I^m \rangle = \frac{\left(\Phi_n/M\right)^m \Gamma(M+m)}{\Gamma\left(M\right)} \tag{14}$$

$$F_m = \Gamma(M+m)/\Gamma\left(M\right)/M^m \tag{15}$$

The first and second moments, $< y >= \Phi_n$ and $\sqrt{\langle y^2\rangle - < y >^2} = \Phi_n/\sqrt{M}$, completely define the statistics of $\widehat{\Phi}_n$ in terms of Φ_n. The fractional moments for $M = 1$ reduce to $F_m = m!$.

In the following analysis ideal realizations will be used. However, the statistics of real data deviate significantly from Gaussian. Even so, experience and analysis, e. g. *Kokoszka and Mikoschb* [2000], show that the Gaussian results apply more broadly. Figure 1 is a plot of the PDF of y/Φ, which represents the scaled periodogram error relative to the mean. The Gaussian distribution, which is the large-M limit, is overlaid in red. The plot shows that for $M < 10$ there is a significant difference between the most probable value, denoted by the red pentagram, and unity mean. Averaging the periodogram estimates brings the most probable value closer to the desired true mean.

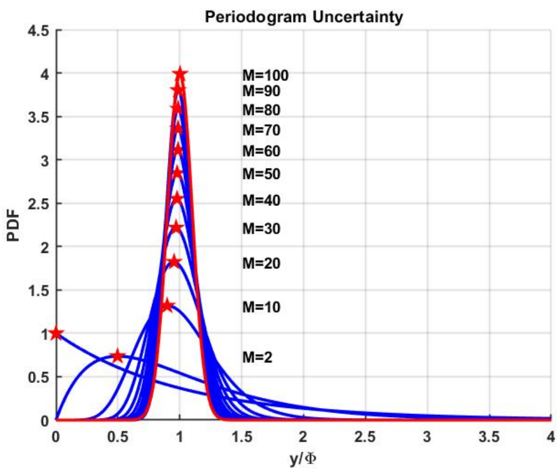

118 **Figure 1.** Probability distribution of y/Φ_n (blue) with gaussian limiting form overlaid (red).

3 Wavelet-Based Spectral Estimation

A complete treatment of wavelets can be found in the text books by Mallat *Mallat* [2009] or *Strang and Borre* [1997]. Wavelets measure structure scale, s, as a function of the position within a segment as opposed to the Fourier domain frequency, $(2\pi/s)$, which applies to the entire segment. The limitations of position-dependent scale measurements are manifest in the wavelet transformations. The continuous wavelet transformation (CWT)is defined as

$$\begin{aligned} F_w(s,y) \qquad &= \textstyle\int_{-\infty}^{\infty} F(y')\frac{1}{\sqrt{s}}w(\frac{y'-y}{s})\,dy' \\ &= \textstyle\int_{-\infty}^{\infty} s\widehat{F}(q)\widehat{w}\,(sq)\exp\{iqy\}\,\frac{dq}{2\pi}. \end{aligned} \tag{16}$$

The Fourier-transform relation is typically used to evaluate the CWT numerically. Wavelets have the following defining properties:

$$w(s) \;=\; 0\;for\;\;|s| > 1/2 \tag{17}$$

$$\int_{-1/2}^{1/2} w(s)ds \;=\; 0 \tag{18}$$

$$\int_{-1/2}^{1/2} |w(s)|^2\,ds \;=\; 1 \tag{19}$$

$$\int_{-\infty}^{\infty} |\widehat{w}(q)|^2\,\frac{dq}{q} \;<\; \infty \tag{20}$$

The final property ensures that the CWT is invertible. At each wavelet scale the CWT is a formally a convolution with a wavelet with finite support over the supported scale range.

The discrete wavelet transform (DWT) extracts only octave-spaced wavelet scale estimates at $s = \Delta y 2^j$ for $j = 1, 2, ..., J$ where J is the largest power of 2 that equals or exceeds N, i. e. $2^J \geq N$. Each DWT wavelet is applied to the even number of samples that span the wavelet. The wavelet scale is defined by j with $j = 1$ corresponding to largest scale, which is usually discarded. The number of wavelet contributions varies with the scale index, j. For $j = 2$, $n = 1$ and 2 corresponding to the centers of two half segments. The smallest wavelet scale contributes $N/2$ centered samples. A discrete wavelet contribution requires a minimum of two data samples. The spatial frequency associated with the structure scale, s, is $q = 2\pi/s$. The DWT,

$$d_n^j = \frac{1}{2}\sum_{k=0}^{N-1} F_k \frac{1}{\sqrt{2^{j-1}}} w((k-n)\,/2^{j-1}), \tag{21}$$

can be evaluated with the same efficiency as the DFT by using an elegant multi-filtering operation described in the cited text book references.

Because the wavelet transform is a linear operation applied to a zero-mean Gaussian process, d_n^j, like its periodogram counterpart, is a zero-mean Gaussian process. Moreover, from the spectral domain form of the CWT it can be shown that

$$\langle F_w(s,y)F_w(s,y+\Delta y)\rangle = \int_{-\infty}^{\infty} \Phi\,(q)\,|s\widehat{w}\,(sq)|^2 \exp\{iq\Delta y\}\,\frac{dq}{2\pi}. \tag{22}$$

From the statistical homogeneity assumption it follows that $\left\langle \left|d_n^j\right|^2 \right\rangle$ is independent of n. The wavelet scale spectrum, as introduced by Hudgins *Hudgins et al.* [1993], is a summation over the contributing wavelet estimates at each scale, formally

$$S_j = \frac{1}{2^{j-1}}\sum_{n=1}^{2^{j-1}} \left|d_n^j\right|^2. \tag{23}$$

Upon substituting (2) into (22), it follows that

$$\left\langle |d_j|^2 \right\rangle = C_s \left\{ \begin{array}{ll} B_1(\ \eta_1, q_0) s^{-\eta_1} & for\ s \leq q_0 \\ B_2(\ \eta_2, q_0) q_0^{\eta_2-\eta_1} s^{-\eta_2} & for\ s > q_0 \end{array} \right. , \tag{24}$$

where

$$B_1(\ \eta_1, q_0) = 2 \int_0^{q_0} u^{-\eta_1} \left|\widehat{w}\,(u)\right|^2 \frac{du}{2\pi}, \tag{25}$$

and

$$B_2(\ \eta_2, q_0) = 2 \int_{q_0}^{\infty} u^{-\eta_2} \left|\widehat{w}\,(u)\right|^2 \frac{du}{2\pi}. \tag{26}$$

We will show with examples that $B_1(\ \eta_1, q_0)\ \sim\ B_2(\ \eta_1, q_0)\ \sim\ 1$, which implies that $\left\langle |S_j|^2 \right\rangle = \Phi_j$. We show that the variance of the wavelet scale spectrum estimates decrease with increasing spatial frequency, but the statistics are distinctly different from the χ_D distribution that applies to sums of independent spectral estimates. Unfortunately, we have no characterization of the wavelet scale spectra PDF.

4 Realization Examples

Realizations defined by (8) have been generated with $N = 4096$ samples spanning 100 km. The sample interval, $\Delta y = 24.41$ m, and the 100-km extent define the positive spatial frequency range from $\Delta q = 2\pi/10^5$ to the Nyquist frequency $q = \pi/\Delta y$. The sampling and spatial extent were chosen to be representative of ionospheric diagnostic measurements. Because realizations generated by (8) are zero-mean and periodic, there are no end-point discontinuities that would otherwise introduce side-lobe contamination.

Periodogram estimates defined by (4) and scale-spectrum estimates defined by (23) were generated from 1000 realizations for an SDF with $\eta = 2$ and for a two-component SDF with $\eta_1 = 1.5$, $\eta_2 = 2.5$, and $q_0 = 2\pi/3000$. A constant value $C_s = 10$ was used for all the realizations. The constant value of C_s is not restrictive because realizations can be scaled without changing the underlying statistics. For the DWT computation a folded replica of the realization is used to eliminate discontinuities in the last contributing wavelet. Any edge contamination is confined to the wavelet contributing to the largest segment distance.

Figure 2 summarizes the scaled periodogram and scale-spectrum estimates for the two-component realizations. The overlaid cyan curves in the upper frame are the 2047 scaled periodogram estimates spanning the resolved spatial frequency range. The overlaid cyan curves in the lower frame are 11 of the 12 octave-spaced scaled scale-spectra estimates, starting with the second resolved scale. The solid red curves are the defining theoretical SDFs. There appears to be less periodogram fluctuation about the mean in the low-frequency range, which is a consequence of the decreasing number of contributing logarithmically-spaced frequency samples. We will show that the periodogram fluctuation statistics about the mean are identical at all frequencies. This is in sharp contrast to the wavelet scale spectrum estimates, which have very small variation at the higher frequencies. The scale spectrum error progressively increases to complete uncertainty at the lowest-resolved spatial frequency.

To explore the statistics of the periodogram and scale-spectra SDF estimates, 100-realization averages were used to compute the means and the second and third fractional moments. The results are summarized in Figures 3 and 4. Because the periodogram measures are frequency independent, only the average values over the frequency ranges are shown together with the expected theoretical values in predicted by (15) in parentheses. As already noted, there is no complementary PDF model for the wavelet scale spectra. The measured second and third fractional moments are listed next to the average

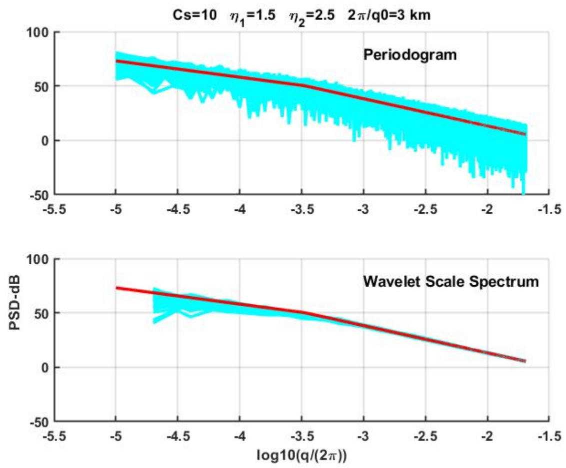

184 **Figure 2.** Periodogram upper frame (cyan) and scale spectrum lower frame (cyan) estimates
185 from two-component power law SDF realizations. The solid red curves show the initiating SDF.

scale spectra samples plotted as red circles. The wavelet fractional moments decrease rapidly to near unity with increasing frequency, which quantifies the observation that wavelet scale spectra estimates are much more certain at the higher frequencies. However, the moments differ significantly from χ_D where $D = 2N_j$, which would be expected for averaged independent spectral estimates. All the measured moments are nearly identical for the single and two-component realizations.

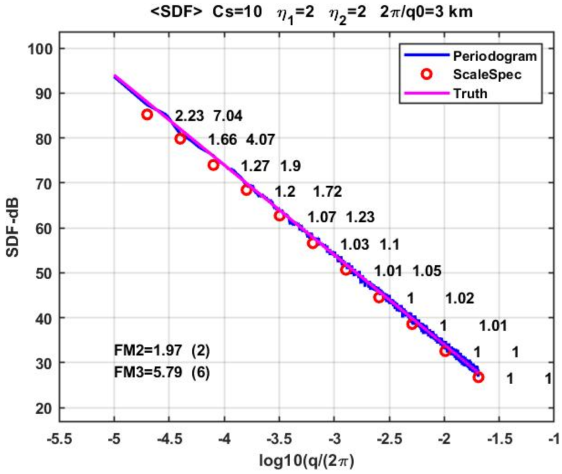

Figure 3. Summary statistics for single power law with $\eta = 2$.

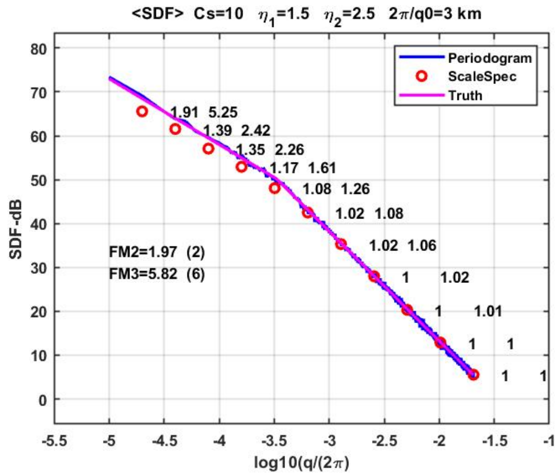

Figure 4. Summary statistics for two-component power law.

5 Logarithmic Transformation

Because of the linear dependence of the logarithm of power-law segments on the logarithm of frequency, it is natural to base estimates of the defining power-law parameters on logarithmic transformations of spectral estimators. Log linear least-squares estimation (LSE) has been analyzed and reported in a paper by *Vaughan* [2005]. The blue curve in Figure 5 is the average of 100 estimates of $\log_{10}\left(\widehat{\Phi}_n\right)$ versus $\log_{10}(q/(2\pi))$ for the $\eta = 2$ SDF. Aside from the -2.48 dB bias, which can be predicted and removed as shown by *Vaughan* [2005], the results suggest that LSE should recover the C_s and η parameters. The wavelet-scale estimates (red circles) show negligible bias at large frequencies, with a progressive increase to a larger bias than the log periodogram estimate at the lowest frequency.

Figure 6 summarizes three sets of LSE estimates. The blue circles are derived from periodogram LSE estimates, which are in agreement with *Vaughan* [2005], although in Figure 6 the bias has not been removed. The cyan circles are derived from scale-spectra

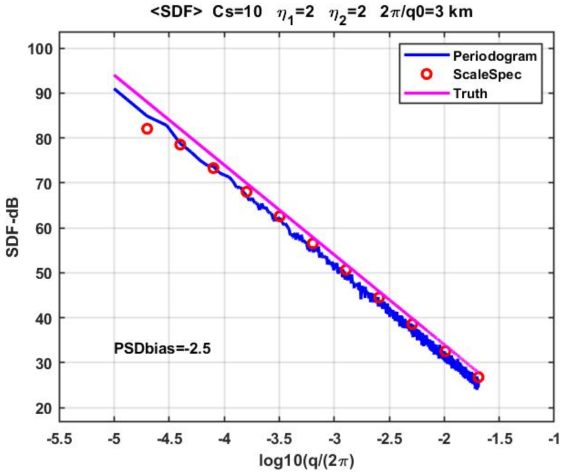

Figure 5. Mean of logarithm of spectral estimates for $\eta = 2$.

estimates over the full scale range. The scale-spectra results have a smaller bias, but larger uncertainty. However, knowing that the scale spectra uncertainty increases with decreasing frequency, the highly uncertain estimates can be eliminated. The red circles show the scale-spectra results derived from scale-spectra estimates constrained to the more certain large-scale range. The constrained LSE results with scale spectra are comparable to the periodogram estimates.

The distinguishing characteristic of all the LSE estimators is the correlation of the $CsdB$ and η estimates. Formally, the uncertainty ellipse is rotated and displaced from its the true value. The blue line is the least-squares fit to the unconstrained periodogram estimates. The log-linear correlation perfectly reproduces the correlation found in the C/NOFS data reported in *Rino et al.* [2016] and other LSE-based estimates. This shows that the ubiquitous coupling regularly observed in LSE estimates is a measurement artifact, not a characteristic of the structure generation process.

If the measurement objective is to estimate the defining power-law parameters, it is necessary to have enough measurements to identify the uncertainty ellipse, whereby the center can be estimated and any known bias corrected. However, if that many independent samples are available, reducing the uncertainty before applying LSE is more effective. This is illustrated in Figure 7. The upper frame repeats the periodogram results shown in Figure 6 for reference. The second and third frames show the improvements realized with LSE $M = 2$ and $M = 10$ pre-averaged periodogram estimates. Averaging scale-spectra estimates does not improve the results, evidently because the low-frequency errors are not reduced significantly.

The larger challenge is accommodating two-component power law processes, which introduces two-more unknowns. The scheme that was used to analyze the C/NOFS data reported in *Rino et al.* [2016] applied two LSE fits to partitions with increasing break points. The smallest overall LSE was selected. The problem with this approach, in retrospect, is that it captures and exaggerates the $CsdB$-η correlation.

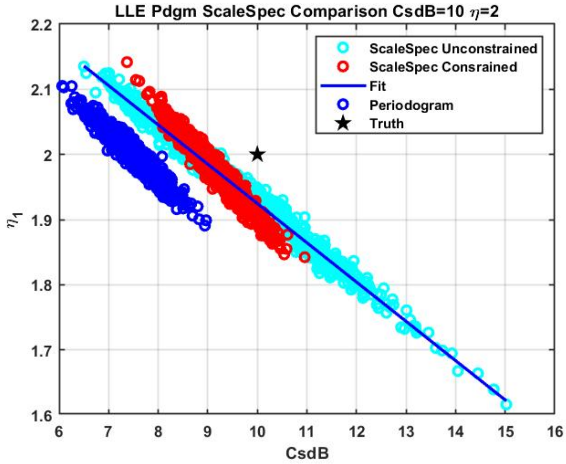

Figure 6. Scatter diagrams of power-law log least-squares parameter estimates from periodogram (blue) and scale spectra estimates for a single-component $\eta = 2$ power law unconstrained (cyan) and constrained (red). The solid line is a leas-squares fit to the scale spectra estimates.

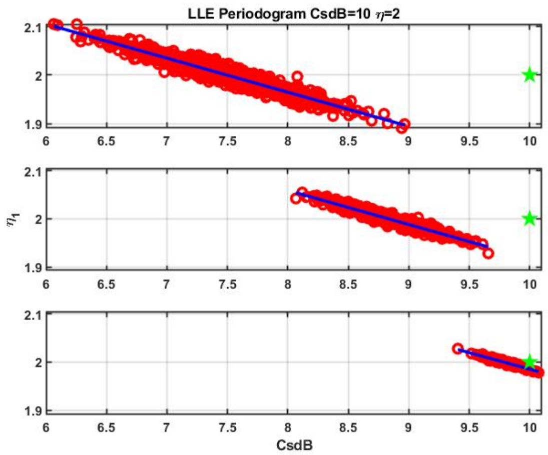

Figure 7. Scatter diagrams of power-law parameters derived with LSE applied to $M = 1$), (non-averaged)$M = 2$ and $M = 10$ pre-averaged periodogram estimates.

6 Irregularity Parameter Estimation

IPE was introduced in *Carrano and Rino* [2016] to estimate parameters that characterize intensity scintillation SDFs. The power-law parameters characterize path-integrated phase, which cannot be measured directly. However, IPE requires only an analytic representation of the expectation of the measured SDF. The parameters that define the expectation SDF, Φ, are adjusted to mach an SDF estimate, $\widehat{\Phi}$. The LLE goodness-of-fit measure

$$\varepsilon^2(\widehat{\Phi}_n|\Phi_n) = \frac{1}{N}\sum_n \left(\log \widehat{\Phi}_n - \log \Phi_n\right)^2, \tag{27}$$

requires no knowledge of the $\widehat{\Phi}_n$ statistics, and it has been used successfully for estimating intensity SDF parameters. This section will consider a more robust maximum-likelihood-procedure introduced by *Carrano et al.* [2017].

Rewriting (13) as

$$\begin{aligned} P(\widehat{\Phi}_n^{(M)}|\Phi_n) &= \Big[M(\widehat{\Phi}_n^{(M)}) - M\log(M\widehat{\Phi}_n^{(M)}/\Phi_n) \\ &\quad + \log(\widehat{\Phi}_n^{(M)}) + \log\Gamma(M)\Big], \end{aligned} \tag{28}$$

the probability of observing a sequence of independent SDF estimates is $\prod_n P(\widehat{\Phi}_n^{(M)}|\Phi_n)$. Logarithm transformation converts the product to the summation:

$$\begin{aligned} \Lambda(\widehat{\Phi}_n^{(M)}|\Phi_n) &= -\log\prod_{n=1}^{N} P(\widehat{\Phi}_n^{(M)}|\Phi_n) \\ &= \sum_{n=1}^{N}\Big[M(\widehat{\Phi}_n^{(M)}) - M\log(M\widehat{\Phi}_n^{(M)}/\Phi_n) \\ &\quad + \log(\widehat{\Phi}_n^{(M)}) + \log\Gamma(M)\Big]. \end{aligned} \tag{29}$$

A maximum likelihood estimate (MLE) is obtained by adjusting the defining Φ_n parameters to minimize (29), which maximizes the likelihood that Φ_n generated the realization.

For a single-component power law, the parameters that minimize (29) can be computed analytically, as demonstrated by *Vaughan* [2010] and *Barret and Vaughan* [2011]. Moreover, the statistical theory establishes bounds on the covariance matrix of the MLE parameter estimates. Indeed, covariance calculations by *Barret and Vaughan* [2011] confirm the C_s-η correlation, who also introduced the Nelder-Mead algorithm *Olsen and Nelsen* [1975] for minimizing (29). The Nelder-Mead algorithm requires initiation with parameters close to the true minimum. Moreover, convergence is sensitive to the number of parameters being estimated and the characteristics of the multi-dimensional object function being minimized. We follow Barret's procedure, but note that one has some latitude in constructing the object function. For example, the minimization can vary either C_s or the logarithm of C_s. Given the log-linear relation between the turbulent strength and the power-law index exploited in (27), one might expect better convergence by varying CdB.

The difference between the log-likelihood prior to minimization and the log-likelihood for the true SDF is introduced as a measure of log-likelihood uncertainty:

$$\Delta\Lambda = \Lambda(\widehat{\Phi}_n^{(M)}|\Phi_n^T) - \Lambda(\Phi_n^T|\Phi_n^T), \tag{30}$$

where the T superscript indicates the true realization SDF. Figure 8 shows a comparison of $\Delta\Lambda$ histograms for the single-power-law realizations with $M = 1$ and $M = 2$. Because Λ is minimized for each $\widehat{\Phi}_n^{(M)}$ estimate, the negative values in the right frame of Figure 8 have no particular significance. Consistent with Figure 1, Figure 8 shows that averaging as few as two SDF estimates significantly reduces the $\Delta\Lambda$ variation. The $\Delta\Lambda$ variation for two-component realizations shows identical behavior. With regard to the Nelder-Mead algorithm, Figure 9, compares the cumulative distributions of the number of iterations to Nelder-Mead convergence with varying C_s and $CsdB$. For these calculations the Matlab implementation of the Nelder-Mead simplex algorithm was used.

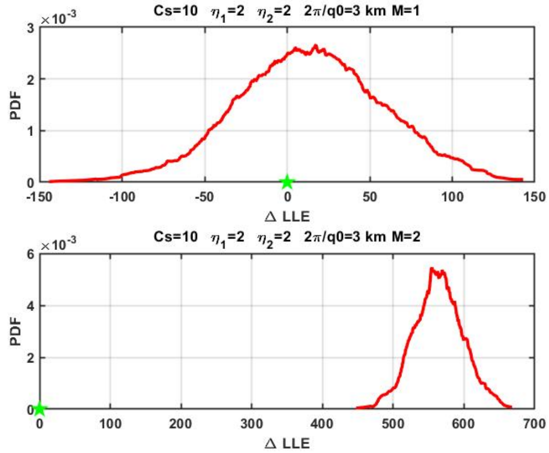

Figure 8. Offset ΔLLE histograms for single power law realizations with $M = 1$ (upper frame) and $M = 2$ (lower frame).

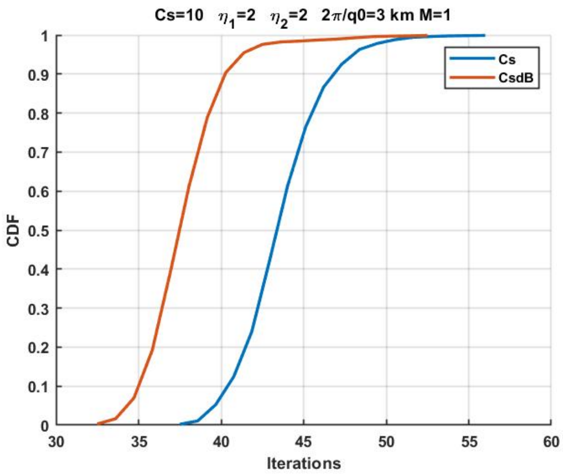

Figure 9. Comparison of Nelder-Mead iterations to convergence with varying C_s and $C_s dB$.

Figure 10 shows the MLE parameters for a single power law with $M = 1$. The Nelder-Mead search was initiated with the LLE estimate. We see that upon comparison to the LLE results, MLE removes the C_s bias and significantly reduces statistical uncertainty. The right frame shows that the C_s-η correlation persists, although the correlation is imperceptible in the summary results. These results are in complete agreement with results reported by *Vaughan* [2010] and *Barret and Vaughan* [2011]. For the single-power law realization processes with no averaging minimizing the object function by varying C_s or $CsdB$ has little effect on the uncertainty and $C_s - \eta$ correlation. As an overall check on performance the Nelder-Mead search was initiated with the true parameter values. The differences, including convergence are imperceptible.

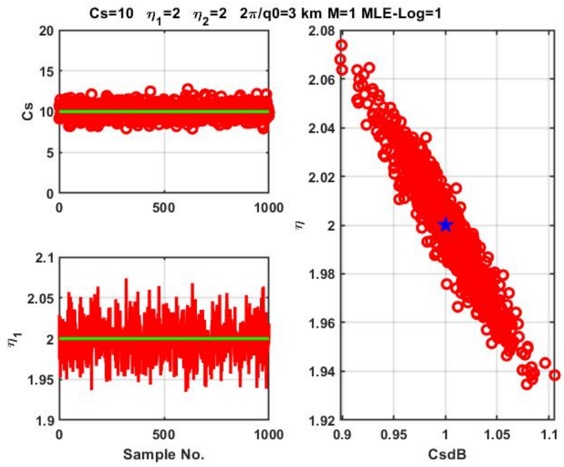

Figure 10. Left frames show MLE parameters for single power-law $M = 1$. Right frame show $\eta - C_s dB$ correlation.

Two-component power-law estimation requires four-parameter initiation. To this end, a mid-frequency q_0 estimate is selected, which partitions $\widehat{\Phi}_n^{(M)}$ into two contiguous sets. Log-linear least-squares estimation is applied to each segment, with a final adjustment to enforce equality at the break scale. For the two-component power-law realizations there is a significant improvement in both parameter error reduction and Nelder-Mead convergence when the search is performed on $CsdB$. Figure 11 shows the estimated parameters for $M = 1$. As with the single power-law results, the same end result is obtained when the search is initiated with the true parameters. The η_1, η_2, and $2\pi/q0$-km parameters are unbiased.

The C_s parameter estimates are more variable. However, the mean of the estimates is the correct value. To explore this further, Figure 12 shows a histogram of the C_s estimates (blue) with the exponential PDF overlaid in read. Evidently the C_s fluctuations are capturing the exponential distribution of the periodogram SDF estimate. Figure 13 shows a scatter diagram of the $\eta_{1,2}$ parameter estimates versus $C_s dB$. The $C_s dB - \eta_1$ correlation persists. However, as with the single-power-law realizations, the $\eta_1 - C_s dB$ correlation is imperceptible in the individual parameter fluctuations. There is no correlation between $CsdB$ and the η_2 parameter estimates. Significant improvements are realized with averaging.

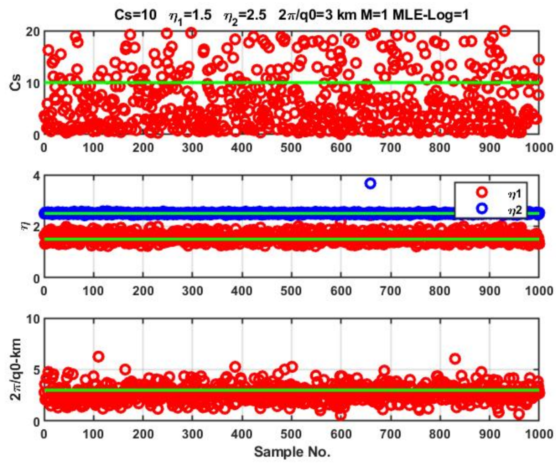

Figure 11. MLE parameters for $M = 1$ two-component power-law realizations.

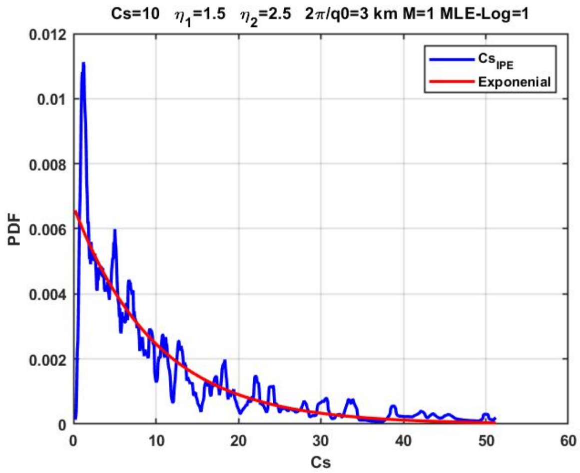

Figure 12. Two-component C_s parameter histogram (blue) with exponential distribution overlaid (red).

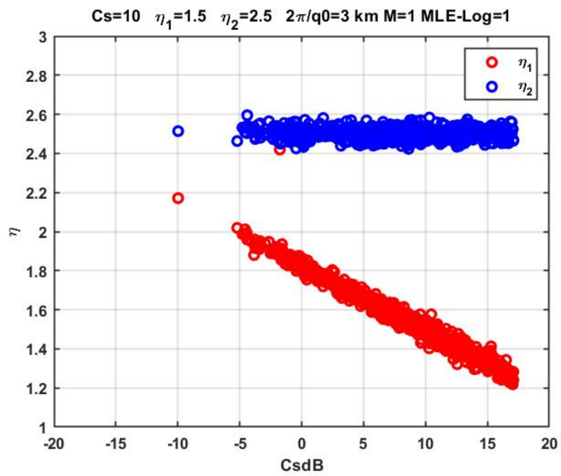

Figure 13. MLE $\eta_{1,2}$ versus C_sdB scatter diagrams for two-component power-law parameters.

7 Discussion and Summary

This paper reviewed LSE and MLE power-law spectra parameter estimation using both periodogram and wavelet-based spectral estimators. All of the procedures generate correlated turbulent strength and large-scale spectral index parameter estimates. The correlation has been noted in in-situ and remote ionospheric diagnostics, but incorrectly attributed to the structuring process. MLE estimation removes biases and significantly reduces statistical errors. Correlation between the $CsdB$ and the large-scale index persists. However, the MLE estimate modified to adjust $CsdB$ rather than Cs reduces the Cs and η_1 errors to negligible levels. Even so, correlation can be detected but recognized as intrinsic to parameter estimation.

The fact that using wavelet-scale spectra exaggerates the Cs-η_1 coupling was not expected. It is well know that the dyadic wavelet scale separation is well matched to the continuous fractal property of power-law processes. Our results verify this property, but for parameter estimation scale independence of the error statistics is more important than scale-selective error reduction. It the absence of a PDF model for wavelet scale spectra MLE estimation intractable. However, we note that most wavelet-based structure analysis is based on spatial-domain structure-functions as opposed to spectral-domain measures *Peter and Rangarajan* [2008].

Acknowledgments
The research presented in this paper was undertaken by the authors to correct a miss interpretation in the published C/NOFS analysis. No data were used in the paper. All the results can be reconstructed as described in the paper.

References

Appourchaux, T. (2003), On maximum likelihood estimation of averaged power spectra, *Astronomy and Astrophysics*, *412*, 903904, dOI: 10.1051/0004-6361:20034401.

Barret, D., and S. Vaughan (2011), Maximum likelihood fitting of x-ray power density spectra: Application to high-frequency quasi-periodic oscillations from the neutron star x-ray binary 4u1608-522, *astro-ph.HE*, *1112.0535*, dOI:10.1088/0004-637X/746/2/131.

Carrano, C. S., and C. L. Rino (2016), A theory of scintillation for two-component power law irregularity spectra: Overview and numerical results, *Radio Sci.*, *51*(doi:10.1002/2015RS005903), 789813.

Carrano, C. S., C. L. Rino, and Groves (2017), Maximum likelihood estimation of phase screen parameters from ionospheric scintillation spectra, *15th International Ionospheric Effects Symposium, Alexandria, VA, May 9-11.*

Hudgins, L., C. A. Friehe, and M. E. Mayer (1993), Wavelet transforms and atmospheric turbulence, *Phys. Rev. Letters*, *71*, 3279–3282.

Kokoszka, P., and T. Mikoschb (2000), The periodogram at the fourier frequencies, *Elesiver, Stochastic Processes and their Applications*, *86*, 4979.

Livingston, R., C. L. Rino, J. P. Mcclure, and W. B. Hanson (1981), spectral characteristics of medium-scale equatorial f region irregularities, *86*(A4).

Mallat, S. (2009), *A Wavelet Tour of Signal Processing The Sparse Way*, Elsevier, Inc., Amsterdam.

Olsen, D. M., and L. S. Nelsen (1975), The Nelder-Mead simplex procedure for function minimization, *Technomectrics*, *17*(1), 46–51.

Peter, A. M., and A. Rangarajan (2008), Maximum likelihood wavelet density estimation with applications to image and shape matching, *IEEE Trans Image Process*, *17*(4), 458–468.

Rino, C. L., R. T. Tsunoda, Petriceks, R. C. Livingston, M. C. Kelley, and D. Baker, K (1981), Simultaneous rocket-borne beacon and in situ measurements of equatorial spread f–intermediate wavelength results, *J. Geophys. Res*, *84*(A4), 2411–2420.

Rino, C. L., K. M. Groves, C. S. Carrano, and P. A. Roddy (2016), A characterization of intermediate-scale spread f structure from four years of high-resolution C/NOFS satellite data, *Radio Sci.*, *51*(doi:10.1002/2015RS005841).

Strang, G., and K. Borre (1997), *Linear Algebra, Geodesy, and GPS*, Wellesley-Cambridge Press, Mass.

Vaughan, s. (2005), A simple test for periodic signals in red noise, *Astronomy and Astrophysics*, *431*, 391–403, dOI: 10.1051/0004-6361:20041453.

Vaughan, S. (2010), A bayesian test for periodic signals in red noise, *Mon. Not. R. Astron. Soc.*, *000*, 1–15.

Yokoyama, T. (2017), A review on the numerical simulation of equatorial plasma bubbles toward scintillation evaluation and forecasting, *Prog. Earth Planet. Sci.*,, *4:37*(doi:10.1186/s40645-017-0153-6, 2017).